ARL-TR-9256 ● AUG 2021

DEVCOM ARMY RESEARCH LABORATORY

X-ray Computed Tomography Inspection and Evaluation of Novel Wire Arc Additively Manufactured Maraging Steel Materials

by William H Green, Victor K Champagne, and Aaron Birt

Approved for public release: distribution unlimited.

NOTICES

Disclaimers

The findings in this report are not to be construed as an official Department of the Army position unless so designated by other authorized documents.

Citation of manufacturer's or trade names does not constitute an official endorsement or approval of the use thereof.

Destroy this report when it is no longer needed. Do not return it to the originator.

ARL-TR-9256 ● AUG 2021



X-ray Computed Tomography Inspection and Evaluation of Novel Wire Arc Additively Manufactured Maraging Steel Materials

William H Green and Victor K Champagne
Weapons and Materials Research Directorate,
DEVCOM Army Research Laboratory

Aaron Birt
Solvus Global

Approved for public release: distribution unlimited.

REPORT DOCUMENTATION PAGE

Form Approved
OMB No. 0704-0188

Public reporting burden for this collection of information is estimated to average 1 hour per response, including the time for reviewing instructions, searching existing data sources, gathering and maintaining the data needed, and completing and reviewing the collection information. Send comments regarding this burden estimate or any other aspect of this collection of information, including suggestions for reducing the burden, to Department of Defense, Washington Headquarters Services, Directorate for Information Operations and Reports (0704-0188), 1215 Jefferson Davis Highway, Suite 1204, Arlington, VA 22202-4302. Respondents should be aware that notwithstanding any other provision of law, no person shall be subject to any penalty for failing to comply with a collection of information if it does not display a currently valid OMB control number.
PLEASE DO NOT RETURN YOUR FORM TO THE ABOVE ADDRESS.

1. REPORT DATE *(DD-MM-YYYY)*	2. REPORT TYPE	3. DATES COVERED (From - To)
August 2021	Technical Report	1 August 2020–31 March 2021

4. TITLE AND SUBTITLE
X-ray Computed Tomography Inspection and Evaluation of Novel Wire Arc Additively Manufactured Maraging Steel Materials

5a. CONTRACT NUMBER

5b. GRANT NUMBER

5c. PROGRAM ELEMENT NUMBER

6. AUTHOR(S)
William H Green, Victor K Champagne, and Aaron Birt

5d. PROJECT NUMBER

5e. TASK NUMBER

5f. WORK UNIT NUMBER

7. PERFORMING ORGANIZATION NAME(S) AND ADDRESS(ES)
DEVCOM Army Research Laboratory
ATTN: FCDD-RLW-S
Aberdeen Proving Ground, MD 21005

8. PERFORMING ORGANIZATION REPORT NUMBER
ARL-TR-9256

9. SPONSORING/MONITORING AGENCY NAME(S) AND ADDRESS(ES)

10. SPONSOR/MONITOR'S ACRONYM(S)

11. SPONSOR/MONITOR'S REPORT NUMBER(S)

12. DISTRIBUTION/AVAILABILITY STATEMENT
Approved for public release: distribution unlimited.

13. SUPPLEMENTARY NOTES
ORCID IDs: William H Green, 0000-0001-8772-3946; Aaron Birt, 0000-0001-7566-8388

14. ABSTRACT

The X-ray computed tomography (XCT) technique is a widely applicable and powerful nondestructive inspection modality for evaluation and analysis of geometrical and physical characteristics of materials, especially internal structures and features. XCT is applicable to metals, ceramics, plastics, and polymer and mixed composites, as well as components, assemblies, and materiel. The Weapons and Materials Research Directorate (WMRD) of the US Army Combat Capabilities Development Command Army Research Laboratory has identified additive manufacturing (AM) of certain materials and components as an essential research area. Metals AM with an emphasis on high-strength steel alloys, among other areas like titanium alloys, is an applied R&D area of the Sciences of Extreme Materials Division (SEMD) in WMRD. SEMD is currently investigating the use of wire arc AM methods for producing steel specimens to determine their overall quality given initial processing conditions. Given that steel is much more attenuating than many other materials and some metals, it can be difficult to get good XCT scan results depending on the objects' overall dimensions. XCT scanning parameters and overall protocols used to mitigate very-low-intensity throughput and achieve acceptable scan image results are discussed. XCT image results, including 2-D internal slices at select locations and 3-D sectioned visualizations, are also shown and discussed. In addition, the physical nature of the types of features found in the steel materials and their possible relationship to processing methodology are discussed.

15. SUBJECT TERMS
X-ray computed tomography, XCT, additive manufacturing, AM, wire arc AM, maraging steel, porosity, voids, delaminations, separation of layers

16. SECURITY CLASSIFICATION OF:			17. LIMITATION OF ABSTRACT	18. NUMBER OF PAGES	19a. NAME OF RESPONSIBLE PERSON
a. REPORT	b. ABSTRACT	c. THIS PAGE			William H Green
Unclassified	Unclassified	Unclassified	UU	40	19b. TELEPHONE NUMBER (Include area code) (410) 306-0817

Standard Form 298 (Rev. 8/98)
Prescribed by ANSI Std. Z39.18

Contents

List of Figures iv

List of Tables v

1. Introduction 1

2. Background and Specimen Description 2

3. XCT Scan Method 6

4. XCT Scan Results and Discussion 8

4.1 SG-10 “Tensile” Specimen (SG-10_tensile) 8

4.2 SG-10 “Hatched-Tensile” Specimen (SG-10_hatched-tensile) 17

5. Summary and Conclusions 26

6. References 29

List of Symbols, Abbreviations, and Acronyms 32

Distribution List 33

List of Figures

Fig. 1 Photographs of representative WAAM specimen..... 4

Fig. 2 Photographs of areal faces of steel WAAM specimen SG-10 “tensile”5

Fig. 3 Additional areal faces of steel WAAM specimen SG-10 “hatched-tensile” 6

Fig. 4 3-D sectioned visualizations and corresponding 2-D surface images in interior of specimen SG-10_tensile parallel to its areal faces..... 9

Fig. 5 2-D images of individual porosity/void discontinuities in specimen SG-10_tensile..... 11

Fig. 6 3-D sectioned visualization and corresponding 2-D surface image close to non-ribbed areal surface (a) and ribbed surface itself (b) of specimen SG-10_tensile..... 11

Fig. 7 3-D sectioned visualizations and corresponding 2-D surface images in interior of specimen SG-10_tensile perpendicular to its areal faces in short areal direction..... 14

Fig. 8 Individual porosity/void in middle area (8a), and 3-D sectioned and 2-D surface images showing linear ≈ horizontal discontinuities in bottom half of images (8b) in interior of specimen SG-10_tensile..... 15

Fig. 9 3-D sectioned visualizations and corresponding 2-D surface images in interior of specimen SG-10_tensile perpendicular to its areal faces in long areal direction 16

Fig. 10 Two different examples of short linear approximately vertical discontinuities in interior of specimen SG-10_tensile in 3-D visualizations and 2-D surfaces parallel to end faces 17

Fig. 11 3-D sectioned visualizations and corresponding 2-D surface images in interior of specimen SG-10_hatched-tensile parallel to its areal faces (continued) 20

Fig. 12 3-D sectioned visualization and corresponding 2-D surface image close to non-ribbed areal surface (a) and ribbed surface itself (b) of specimen SG-10_hatched-tensile..... 21

Fig. 13 2-D image of individual porosity/void discontinuity with a maximum dimension of about 1.8 mm in specimen SG-10_hatched-tensile. Note somewhat larger porosity/void almost directly below it..... 22

Fig. 14 3-D sectioned visualizations and corresponding 2-D surface images in interior of specimen SG-10_hatched-tensile perpendicular to its areal faces in short areal direction 23

Fig. 15 Individual porosity/void in middle area (a), and 3-D sectioned and 2-D surface images showing linear approximate horizontal discontinuities (b and c) in interior of SG-10_hatched-tensile 24

Fig. 16 3-D sectioned visualizations and corresponding 2-D surface images in interior of specimen SG-10_hatched-tensile perpendicular to its areal faces in long areal direction 25

Fig. 17 Two different examples of short linear approx. vertical discontinuities in interior of specimen SG-10_hatched-tensile in 3-D visualizations and 2-D surfaces parallel to end faces 26

List of Tables

Table 1 XCT scanning parameters 7

1. Introduction

The X-ray computed tomography (XCT) technique is a widely applicable and powerful nondestructive inspection modality for evaluation and analysis of geometrical and physical characteristics of materials, especially internal structures and features. XCT is applicable to metals, ceramics, plastics, and polymer and mixed composites, as well as components, assemblies, and materiel. The principal advantage of XCT is that it provides densitometric (that is, radiological density and geometry) images of thin cross sections through an object in a noninvasive manner. Because of the absence of structural superimposition, images are much easier to interpret than conventional radiological images. The user can quickly learn to read XCT data because images correspond more closely to the way the human mind visualizes 3-D structures than 2-D projection radiology (that is, film radiography, real-time radiography, and digital radiography).[1–4] The Weapons and Materials Research Directorate (WMRD) of the US Army Combat Capabilities Development Command Army Research Laboratory has identified additive manufacturing (AM) of certain materials and components as an essential research area. Metals AM with an emphasis on high-strength steel alloys, among other areas like titanium alloys, is an applied R&D area of the Sciences of Extreme Materials Division (SEMD) in WMRD.

XCT is an excellent nondestructive evaluation (NDE) method for inspecting these relatively dense and oftentimes geometrically complex materials due to its briefly described capabilities. The SEMD is currently investigating the use of wire arc AM (WAAM) methods for producing steel specimens to determine their overall quality given initial processing conditions. Given that steel is much more attenuating than many other materials and some metals, it can be difficult to get good XCT scan results depending on the object's overall dimensions. Scans through relatively thick and/or large materials or components can produce low-intensity throughput results with low image contrast, low signal-to-noise ratio (SNR), and the presence of image artifacts. These effects present a challenge to obtaining both good or even decent qualitative image results and representative or accurate quantitative analytical results where straightforward image processing, like applying only simple global thresholds, is not sufficient for separating features. XCT scanning parameters and overall protocols used to mitigate very-low-intensity throughput and achieve acceptable scan image results are discussed. XCT image results, including 2-D internal slices at select locations and 3-D sectioned visualizations, are also shown and discussed. In addition, the physical nature of the types of features found in the steel materials and their possible relationship to processing methodology are discussed.

2. Background and Specimen Description

WAAM, which is a variation of a direct-energy deposition technology, is one of the lesser-known metal 3-D printing technologies and uses an arc-welding process to print metal parts. Unlike the more common metal-powder AM processes, WAAM works by melting metal wire using an electric arc as the heat source. Any metal that can be welded can also be used with WAAM.[5] Gas metal arc-welding (MIG/MAG) is the process of choice: the wire is the consumable electrode, and its coaxiality with the welding torch results in an easier tool path. WAAM hardware currently uses standard, off-the-shelf welding equipment, including the welding power source, torches, and wire feeding systems. Motion can be provided by either robotic systems or computer numerically controlled gantries.[6] WAAM processes use commercially available wires produced for the welding industry and available in spooled form and in a wide range of alloys as feedstock materials. Gas metal arc welding is not always the best process for all metals. Depending on the nature of the heat source, there are commonly three types of WAAM processes[7]: MIG/MAG,[8] gas tungsten arc welding–based,[9] and plasma arc welding–based.[10]

WAAM has become a promising fabrication process for various engineering materials such as steel, nickel alloy, titanium, and aluminum. Compared with traditional subtractive manufacturing, WAAM systems can reduce fabrication time by 40%–60% and postmachining time by 15%–20% depending on the component size.[11] Uniquely, since WAAM combines the use of wire and electric arc as a fusion source to build components layer by layer, it can offer significant cost savings compared with powder and alternative fusion sources, such as laser and electron beam, respectively. In addition, a high deposition rate, key for producing such components, is provided while also allowing significant material savings compared with conventional manufacturing processes. However, high-quality production in a wide range of materials is currently limited by the elevated levels of heat input, which causes a number of materials processing challenges in WAAM.[12] Deposition rates approaching 10 kg/h for steels[13,14] is achievable with WAAM, which is approximately 16 times higher than powder-based processes with maximum deposition rates of 600 g/h.[15] Given that higher deposition rate is one of the attractive features of WAAM, control over the relatively large volume of liquid weld metal is critical. The solidification of a large weld pool in WAAM can be correlated with the conventional casting process experiencing differences in solidification behaviors at the center and outer periphery locations of a casting.[16] Compared with laser- and electron-based processes that restrict overall dimensions of an object due to chamber size, WAAM is capable of producing objects without dimensional limits. Thus, high deposition rate and theoretically unlimited metal deposition capability makes WAAM very suitable for production of medium- to

large-scale parts. However, larger bead volumes and higher surface roughness compared with powder-based processes[15] currently restricts its applications to production of low- to medium-complexity parts.[16]

Figure 1 shows digital photographs of a representative WAAM specimen built on a steel base plate showing views of the end, looking down at an angle, and top view. The striated, or ribbed, structure on the outside resulting from the method of material deposition on the base plate is evident. Figures 2 and 3 show digital photographs of both areal faces of maraging steel WAAM specimens SG-10 "tensile" and "hatched-tensile", respectively. Maraging steels are known for superior strength and toughness without losing ductility. These steels are a special class of low-carbon ultra-high-strength steels that derive their strength from precipitation of intermetallic compounds with a principal alloying element of 15%–25% nickel by weight.[17] Both specimens were mechanically sectioned from larger manufactured AM steel build plates similar to that in Fig. 1, so as to be penetrable by the XCT technique. The overall dimensions of the tensile and hatched-tensile specimens were approximately 1 × 2.5 × 4.06 inches (25.4 × 63.5 × 103 mm) and 1 × 2.5 × 4.38 inches (25.4 × 63.5 × 111 mm), respectively. Essentially, the specimens were sectioned to be as large as reasonably possible overall and still allow sufficient penetration, but not high penetration, by 450-kV peak X-rays. Both specimens have the previously noted physical linear ribbed structure on about half of one of their faces, which arise from the WAAM fabrication method.

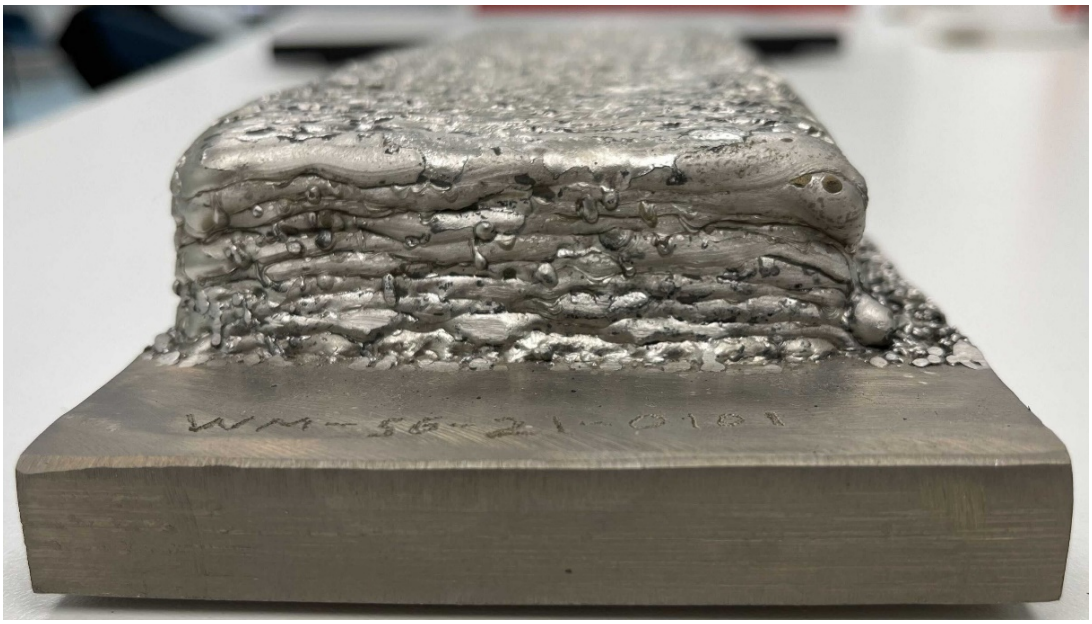

1a. Tilted end view



1b. Top view

Fig. 1 Photographs of representative WAAM specimen

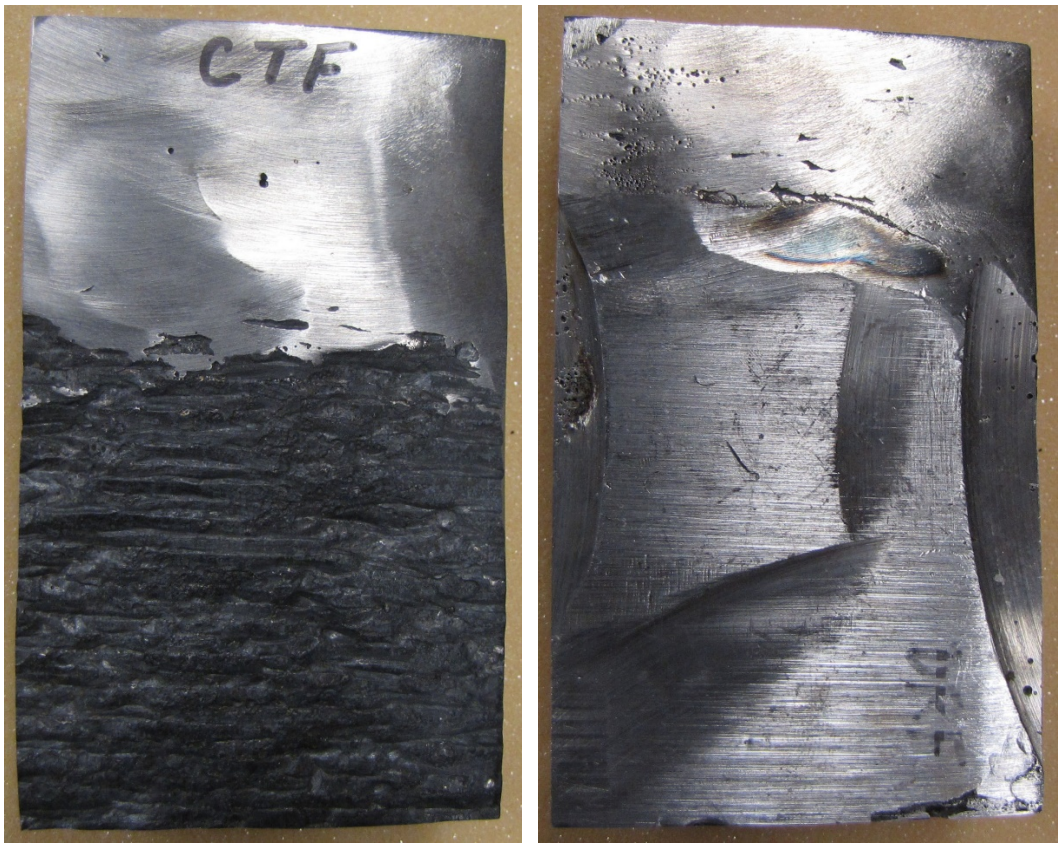

Fig. 2 Photographs of areal faces of steel WAAM specimen SG-10 “tensile”



Fig. 3 Additional areal faces of steel WAAM specimen SG-10 “hatched-tensile”

3. XCT Scan Method

Each specimen was secured within a free-standing foam base such that their areal faces were tilted from the vertical a small amount, and their top and bottom end surfaces were not horizontal. The shorter and longer areal dimensions were horizontal and tilted from the vertical, respectively, which was done to create a lack of parallelism between each specimens top and bottom surfaces and the incoming X-rays. It was also done to ensure that the longest X-ray path length through either specimen during its scan rotation was the shorter areal dimension. The parameters of the XCT technique used to scan the specimens are given in Table 1. Parameters in the table exhibit scanning process steps taken to maximize SNR and image quality while minimizing noise and high X-ray attenuation artifacts, including X-ray beam hardening (source filter), frame averaging, and view (i.e., projection) oversampling. “Hardening” the X-ray beam—that is, selectively lessening or removing altogether lower energy components of a polychromatic beam—generally results in less gray-level variation in reconstructed images, or “cupping”,

due to selective attenuation of lower energies in and of itself. A harder or more monochromatic X-ray beam is more uniformly attenuated by the material of interest since linear attenuation coefficients are dependent on both X-ray energy (also frequency) and material atomic composition.

Table 1 XCT scanning parameters

Parameter	Value
X-ray voltage (peak)	445 kV
X-ray energy (peak)	445 keV
X-ray current	1500 μA
Detector sample rate	4 frame/s (fps)
X-ray focal spot size	400 μm
Source-to-image distance	880 mm
Source-to-object distance	582.5 mm
Magnification	1.51
Detector element pitch	200 μm
Effective pixel pitch	132.4 μm
Unsharpness	1.02 pixels
Frame average	8
No. projections (views)	2000
Source filter (copper)	≈1.59 mm (0.063 inch)
Detector filter (copper)	≈1.59 mm (0.063 inch)

The XCT scan method used eight times (8X) frame averaging and projection image "oversampling" to maximize the detection of density variations within the maraging steel WAAM specimens. When an image with random noise is frame averaged an n number of times, the magnitude of the noise fluctuation is decreased by the factor of the square root of n. In other words, the percent of original random noise remaining after n frames is averaged is $100 * (\frac{1}{\sqrt{n}})$.[18] It is evident from the functionality of this equation that as the number of frames increases, the improvement in noise reduction becomes less and less effective. Thus, although frame averaging does not add a large amount of processing time applied to a few images like a few digital radiographs, there is a tradeoff between image improvement and processing time spent if a relatively large number of images, such as is the case in extensive and/or oversampled XCT scans, will be averaged. A commonly used number of frames averaged is four, which reduces noise fluctuation by 50% because it significantly reduces the noise level in a reasonable amount of processing time for large data sets. In Nyquist–Shannon sampling theory,[19] given a polychromatic (i.e., multiple frequency) temporal (or spatial) continuous function, f(x), with known maximum spatial frequency X_{max}, it is completely determined by giving its sampled ordinates at a series of points spaced less than or equal to a distance of $1/(2X_{max})$ apart. The threshold $2X_{max}$ is called the Nyquist rate and is an attribute of the continuous spatial input f(x) being sampled. The sample rate, R,

must exceed the Nyquist rate for the samples to suffice to represent f(x). The threshold R/2 is called the Nyquist frequency and is an attribute of the sampling equipment. The number of projections used to reconstruct an XCT data set is one of the determining factors in image quality. Too large an interval between projections, or undersampling, results in the loss of accurate information about the physical geometry of the scanned object. Reconstructed images of undersampled WAAM specimens would likely exhibit some type of regular angular variation in gray levels and associated loss of internal and edge physical information. Oversampling the scan space provides finer physical geometric information for the reconstruction process and helps to mitigate the effects of very high X-ray attenuation and related noise in the resultant XCT data. The scans of the specimens purposely collected twice as many projections as normal, which is based on 1.5 times the pixel width of the specimen field of view, to oversample the scan space during the 360° rotation. Application of effective frame averaging and oversampling the scan space are illustrative of the principle of obtaining the best quality XCT data set given the material of interest and overall scan considerations to begin analysis with.

4. XCT Scan Results and Discussion

4.1 SG-10 "Tensile" Specimen (SG-10_tensile)

Three-dimensional densitometric XCT image data sets provide a very powerful and unique method to directly visualize, interpret, and evaluate internal structure and features in materials. Figure 4 shows both 3-D virtually sectioned spatial visualizations and their corresponding 2-D exposed surfaces of SG-10_tensile, including views near (i.e., within a few millimeters of) the face with the ribbed structure and about one-quarter, halfway, and three-quarters of the way through it in the thickness direction. It is readily apparent that there are numerous lower-density discontinuities in the specimen with different shapes, many of them likely being some type or types of porosity and/or voids. Figure 5 shows 2-D images that have selected features with maximum dimensions of about 2.4 mm (5a) and 6.3 mm (5b). Figure 6 shows a 3-D visualization and its corresponding 2-D surface very close to the non-ribbed face of the specimen as well as a visualization of the ribbed structure itself. The striated porosity type features are evident on the right side in the specimen in the top left and right images (6a). Even though there is horizontal structure on the surface in the bottom half of the specimen in the short areal direction, it is difficult to show it clearly in the visualization due to the level of X-ray attenuation by the specimen, as seen in the bottom image (6b).

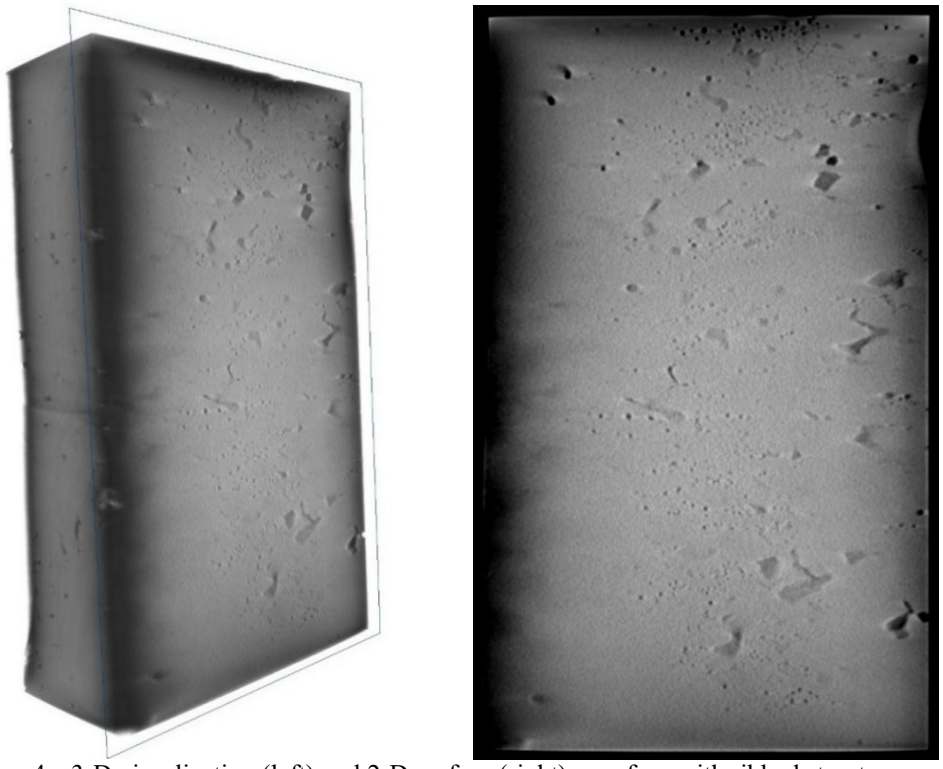

4a. 3-D visualization (left) and 2-D surface (right) near face with ribbed structure

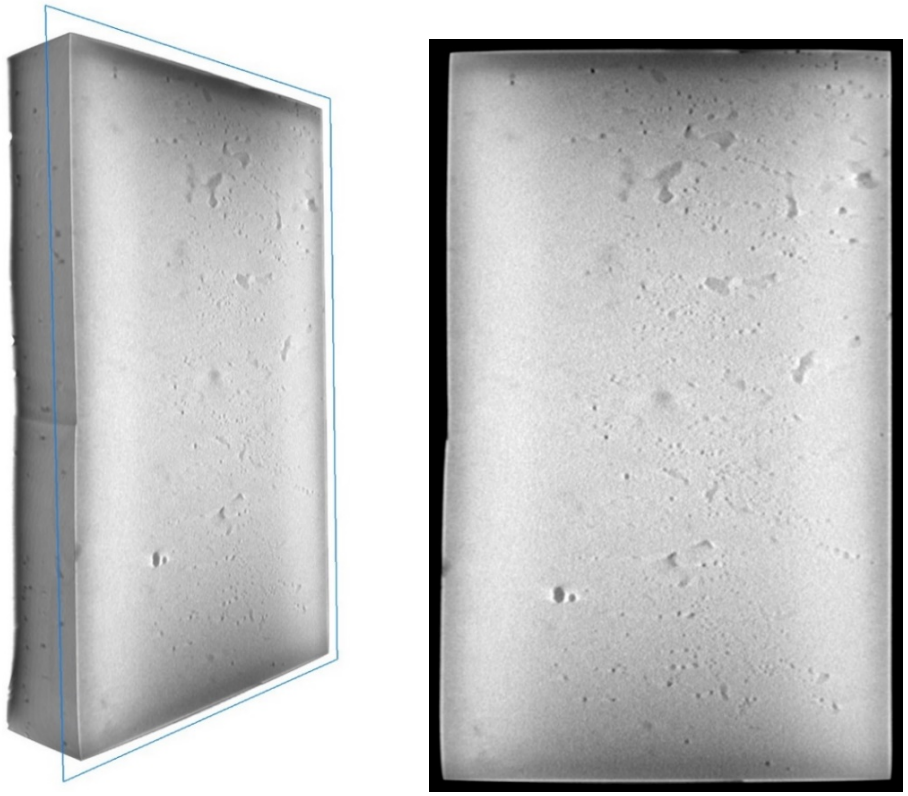

4b. 3-D visualization and 2-D surface about one-quarter of the way through thickness

Fig. 4 3-D sectioned visualizations and corresponding 2-D surface images in interior of specimen SG-10_tensile parallel to its areal faces

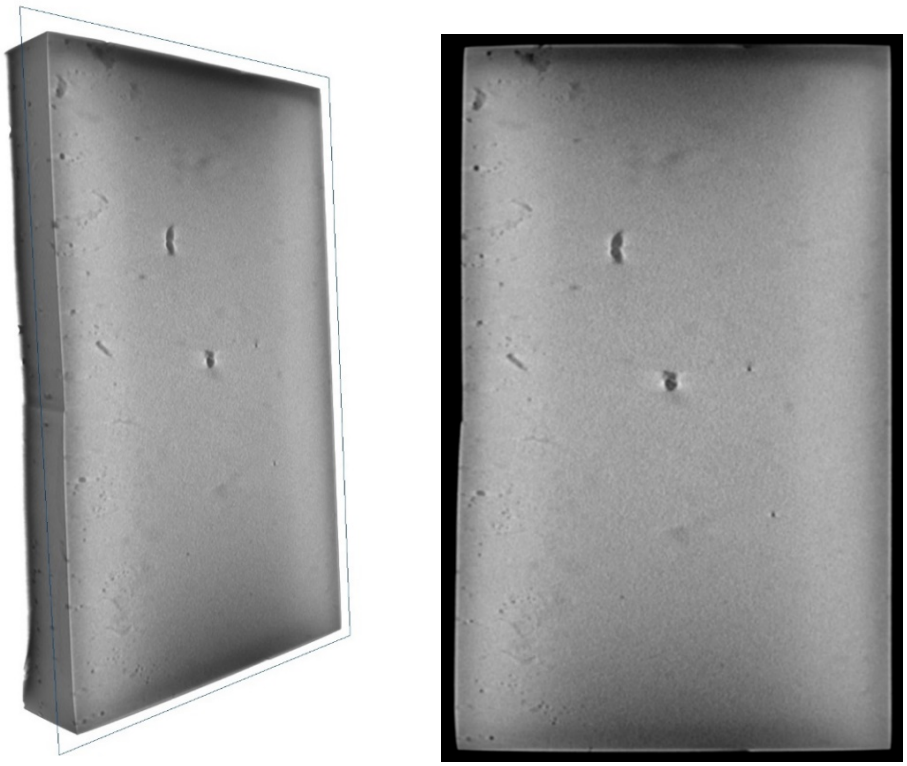

4c. 3-D visualization and 2-D surface about halfway through thickness

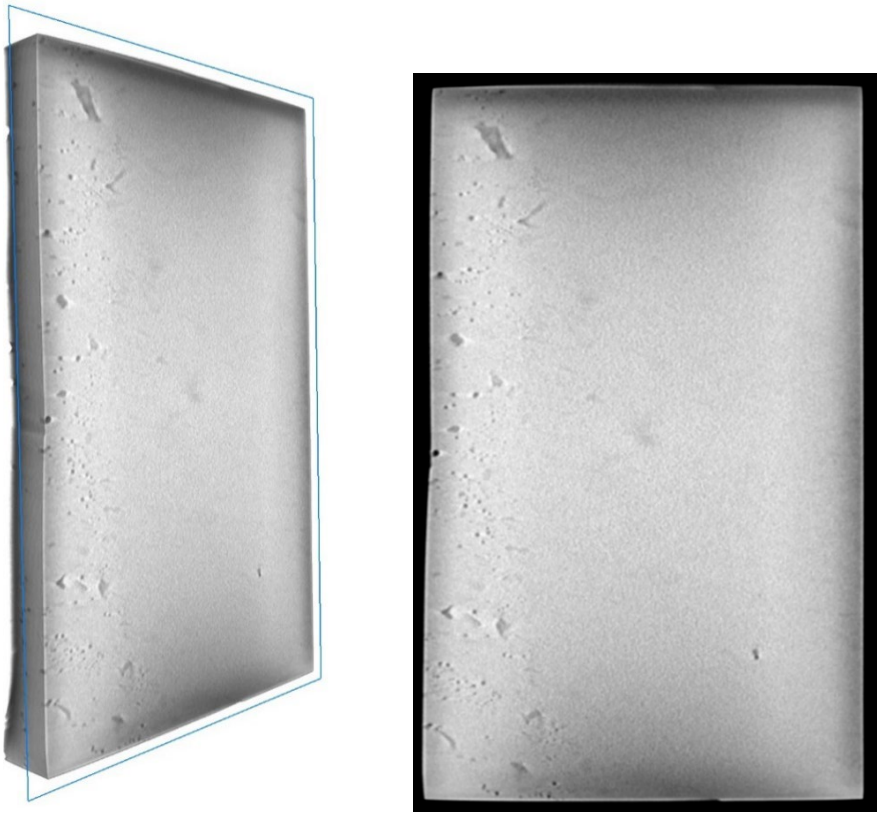

4d. 3-D visualization and 2-D surface about three-quarters of the way through thickness

Fig. 4 3-D sectioned visualizations and corresponding 2-D surface images in interior of specimen SG-10_tensile parallel to its areal faces (continued)

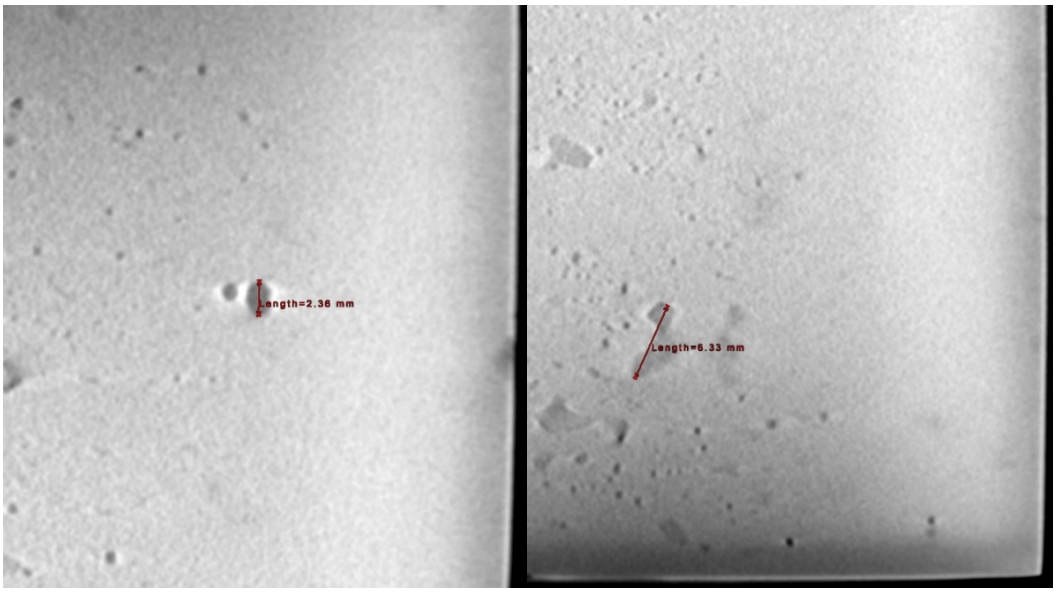

a. Feature w/ maximum dimension of 2.4 mm b. Feature w/ maximum dimension of 6.3 mm

Fig. 5 2-D images of individual porosity/void discontinuities in specimen SG-10_tensile

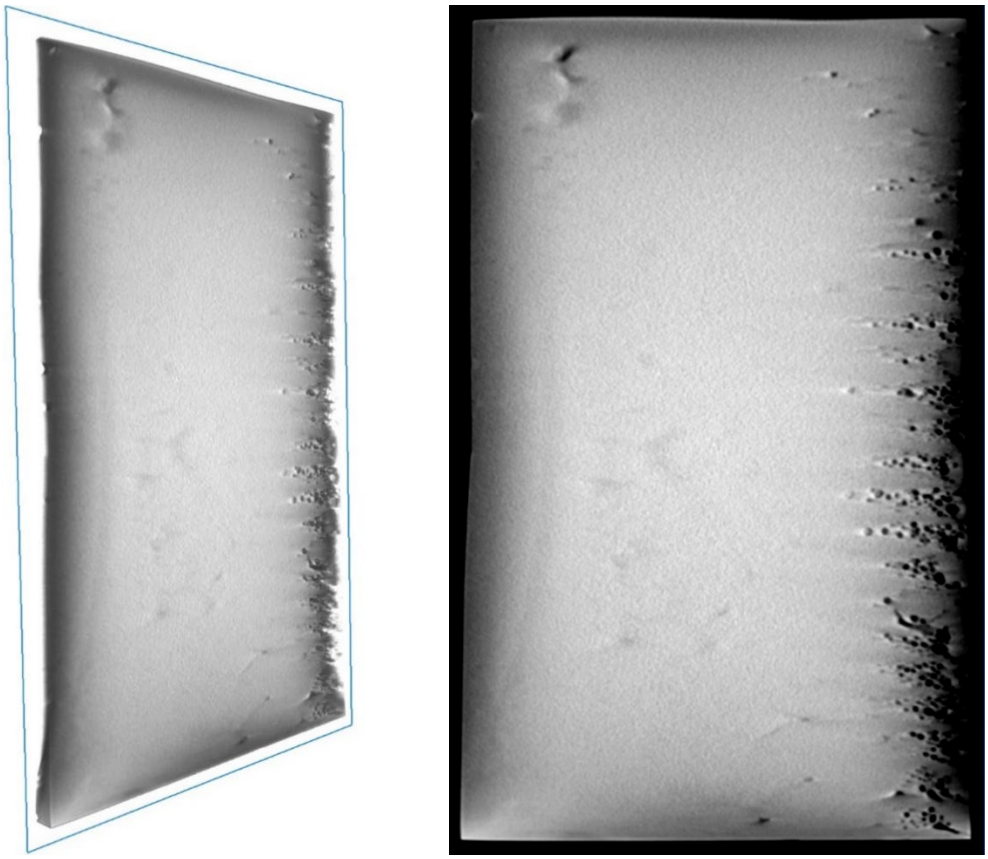

6a. 3-D visualization (left) and 2-D surface (right) very close to non-ribbed areal surface

Fig. 6 3-D sectioned visualization and corresponding 2-D surface image close to non-ribbed areal surface (a) and ribbed surface itself (b) of specimen SG-10_tensile



6b. 3-D visualization of outside ribbed areal surface

Fig. 6 3-D sectioned visualization and corresponding 2-D surface image close to non-ribbed areal surface (a) and ribbed surface itself (b) of specimen SG-10_tensile (continued)

Figure 7 shows 3-D sectioned visualizations and their 2-D surfaces about one-quarter, halfway, and three-quarters of the way through SG-10_tensile perpendicular to its areal faces in the horizontal or "sideways" direction parallel to the short areal dimension. Again, numerous low-density discontinuities are apparent in the specimen. Secondly, examples of essentially linear and approximately horizontal low-density discontinuities can be seen in these views. These features appear to have varying degrees of solid uniformity or connectivity (i.e., "breaks" in the line). Figure 8a shows a 2-D image of an individual feature with a maximum dimension of about 4.7 mm, and 8b a 3-D visualization and 2-D surface of a "group" of linear approximately horizontal features in the lower half of the specimen. Figure 9 shows 3-D visualizations and their 2-D surfaces about one-quarter and halfway through SG-10_tensile perpendicular to its areal faces in the vertical direction parallel to the long areal dimension (9a and b). It also shows a relatively large discontinuity in the same view orientation with its long dimension perpendicular to the areal faces (9c). Once again, numerous low-density

discontinuities are apparent in the specimen. Second, examples of essentially linear and approximately vertical low-density discontinuities can be seen in these views. These features also appear to have varying degrees of solid uniformity or connectivity and are most likely the same or similar features as seen in Figs. 7 and 8 from a perpendicular orientation. Figure 10 shows visualizations and internal surfaces of the specimen in the same orientation exhibiting groups of these vertical discontinuities with the second set of images (10b) sectioned near the bottom of the specimen, which was the end closest to the scanning turntable.

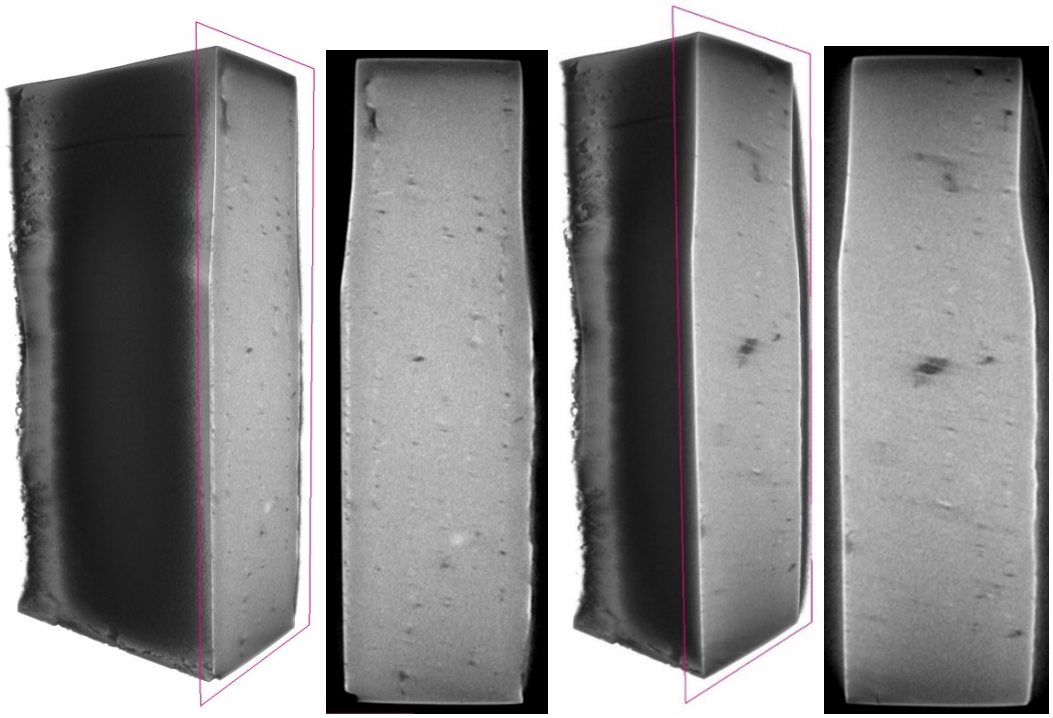

7a. About one-quarter of the way through

7b. About one-half of the way through

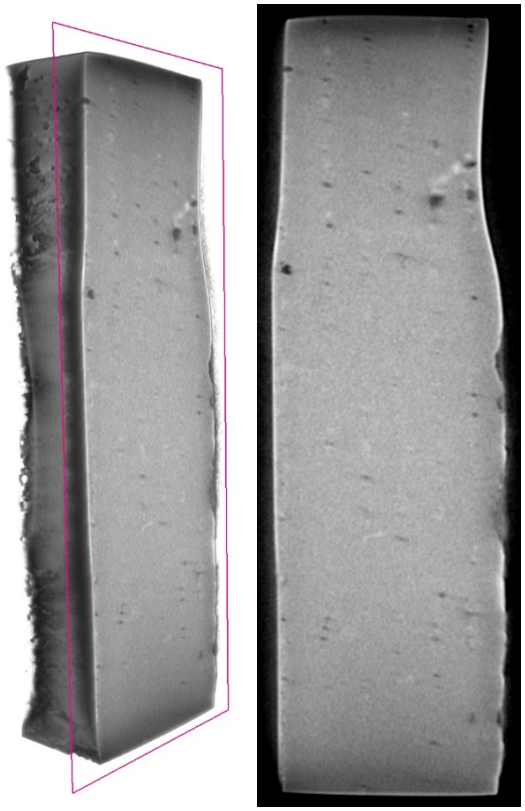

7c. About three-quarters of the way through

Fig. 7 3-D sectioned visualizations and corresponding 2-D surface images in interior of specimen SG-10_tensile perpendicular to its areal faces in short areal direction

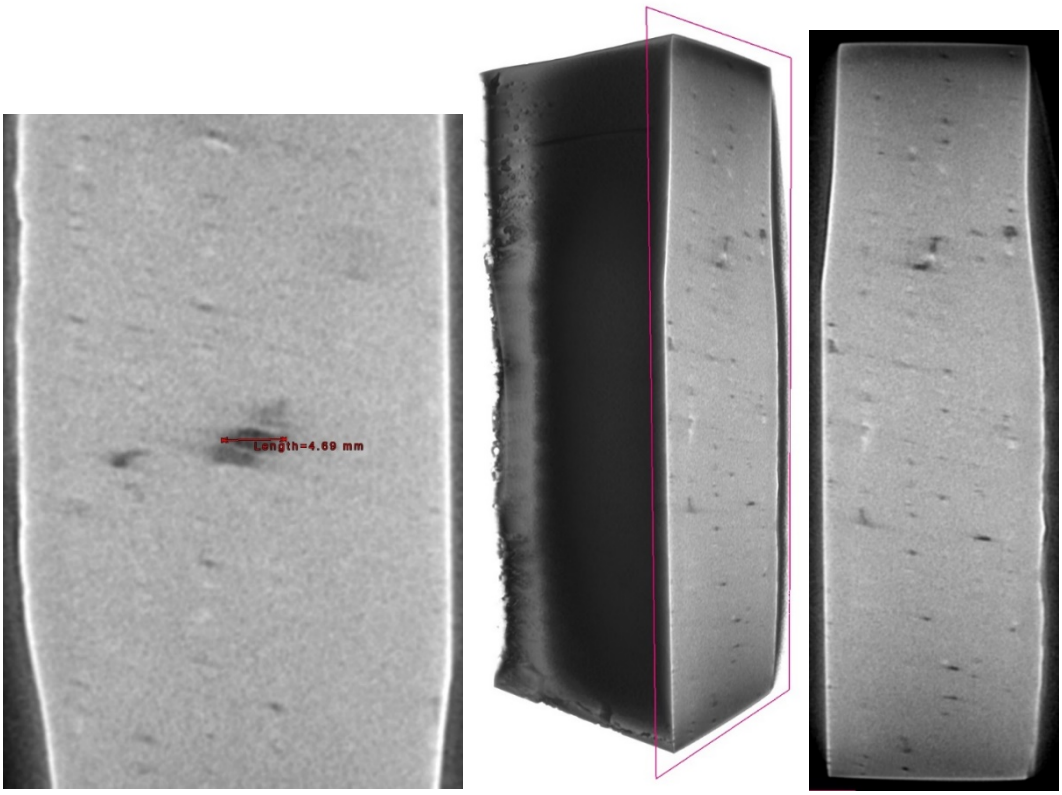

8a. Feature with max dimension of 4.7 mm 8b. 3-D and 2-D images with linear ≈ horizontal features

Fig. 8 Individual porosity/void in middle area (8a), and 3-D sectioned and 2-D surface images showing linear ≈ horizontal discontinuities in bottom half of images (8b) in interior of specimen SG-10_tensile

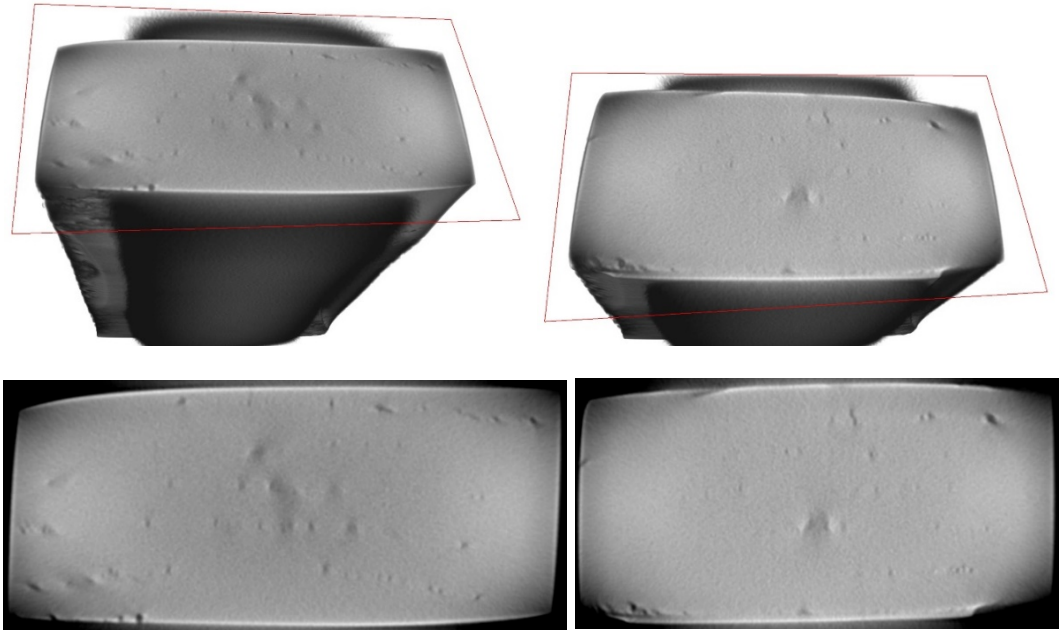

9a. About one-quarter of the way through

9b. About one-half of the way through

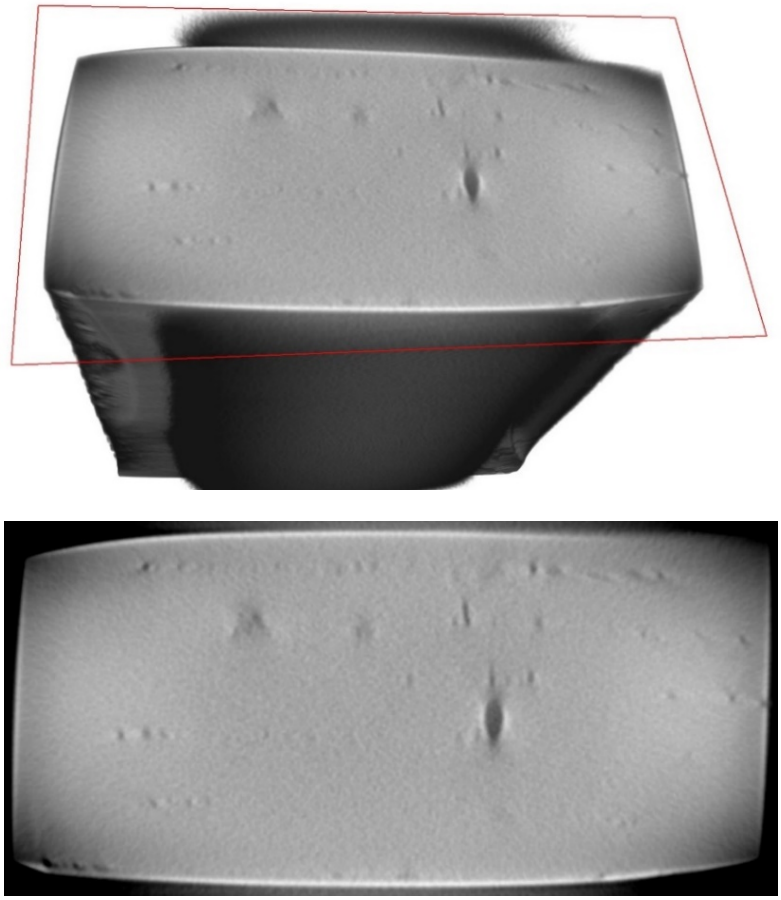

9c. Individual large discontinuity with long dimension perpendicular to areal faces

Fig. 9 3-D sectioned visualizations and corresponding 2-D surface images in interior of specimen SG-10_tensile perpendicular to its areal faces in long areal direction

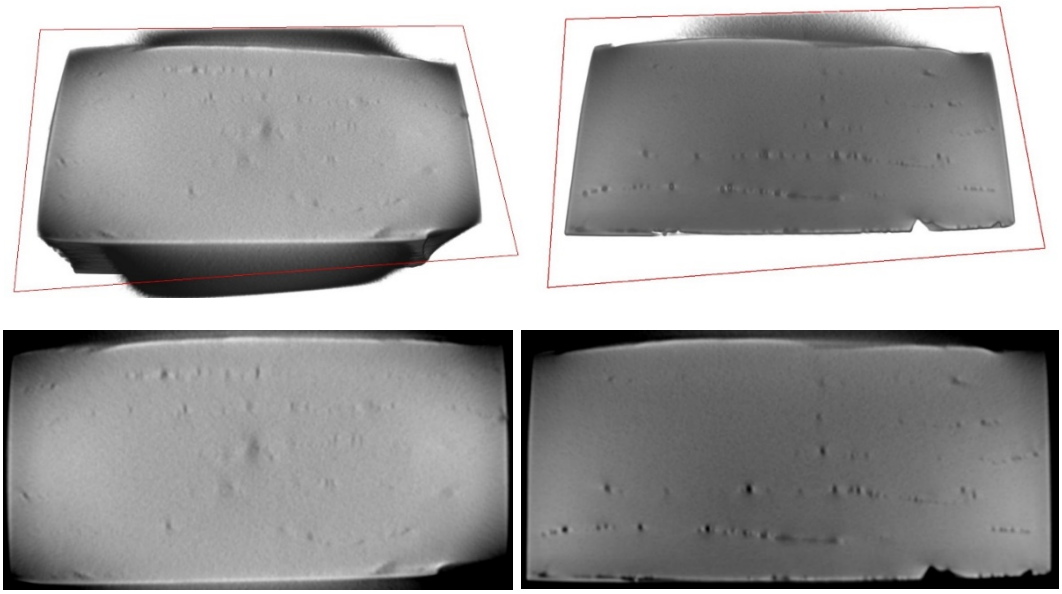

10a. Example of short linear ≈ vertical features near top of images

10b. Example of short linear ≈ vertical features closer to bottom of images

Fig. 10 Two different examples of short linear approximately vertical discontinuities in interior of specimen SG-10_tensile in 3-D visualizations and 2-D surfaces parallel to end faces

4.2 SG-10 "Hatched-Tensile" Specimen (SG-10_hatched-tensile)

Figure 11 shows 3-D virtually sectioned visualizations and their corresponding 2-D surfaces of SG-10_hatched-tensile, including views near (i.e., within a few millimeters of) the face with the ribbed structure and about one-quarter, halfway, and three-quarters of the way through it in the thickness direction. It is apparent that there are a number of lower-density discontinuities with varying shapes in this specimen also, many of them also being some type or types of porosity and/or voids. However, there appear to be qualitatively fewer discontinuities in approximately the same areal space in SG-10_hatched-tensile compared with SG-10_tensile. Figure 12 shows a 3-D visualization and its corresponding 2-D surface close to the non-ribbed face of the specimen (12a), as well as a visualization of the ribbed structure itself (12b). Figure 13 shows a 2-D image having a selected discontinuity with a maximum dimension of about 1.8 mm. The approximate size of this discontinuity is illustrative of features in SG-10_hatched-tensile being smaller than those in SG-10_tensile in general. Figure 14 shows 3-D visualizations and their 2-D surfaces about one-quarter, halfway, and three-quarters of the way through SG-10_hatched-tensile perpendicular to its areal faces in the horizontal direction parallel to the short areal dimension. Again, a number of low-density discontinuities are apparent in the specimen. Second, examples of essentially linear and approximately horizontal low-density discontinuities can be seen in these

views. Again, these features appear to have varying degrees of solid uniformity or connectivity. Figure 15 shows a 2-D image of an individual discontinuity with a maximum dimension of about 1.7 mm (15a) and two examples of 3-D visualizations and corresponding 2-D surfaces of grouped linear horizontal discontinuities (15b). Figure 16 shows 3-D visualizations and 2-D surfaces about one-quarter, halfway, and almost halfway through SG-10_hatched-tensile perpendicular to its areal faces in the vertical direction parallel to the long areal dimension. Once again, a number of low-density discontinuities are apparent in the specimen. Second, examples of essentially linear and approximately vertical low-density discontinuities can be seen in these views. These features also appear to have varying degrees of solid uniformity or connectivity and are most likely features as seen in Figs. 14 and 15 from a perpendicular orientation. The relatively short linear vertical discontinuities in approximately the middle of the images in Fig. 16c appear to almost vertically line up. Figure 17 shows two sets of 3-D visualizations and their 2-D surfaces in the specimen exhibiting groups of these vertical discontinuities. In both sets of images, these features are near their bottoms and are grouped along a near horizontal line. In fact, in Fig. 17b, there are 11 or so individual features in the horizontal group.

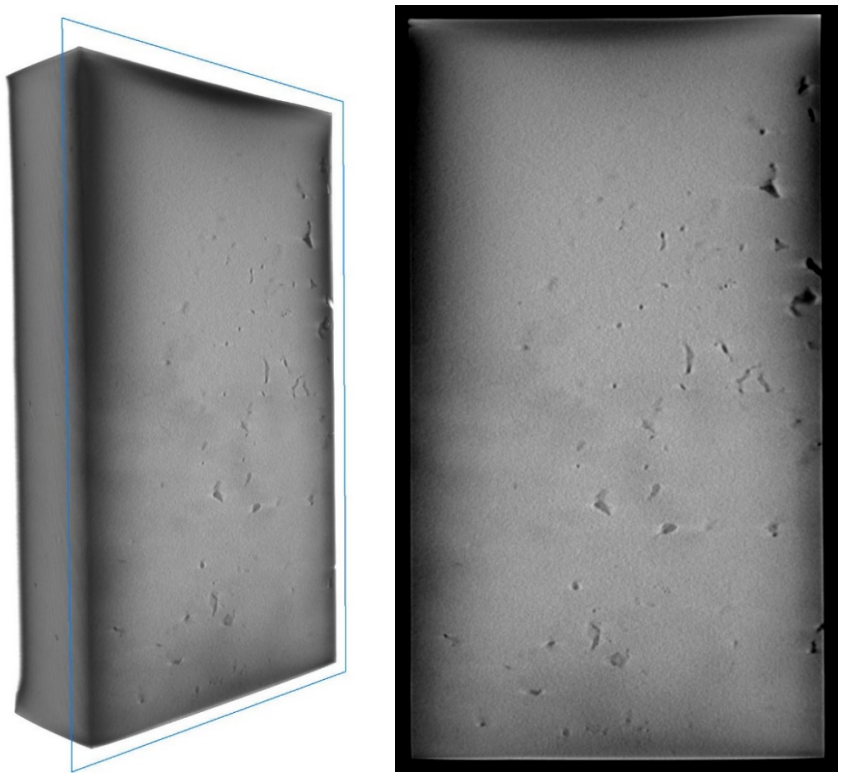

11a. 3-D visualization (left) and 2-D surface (right) near face with ribbed structure

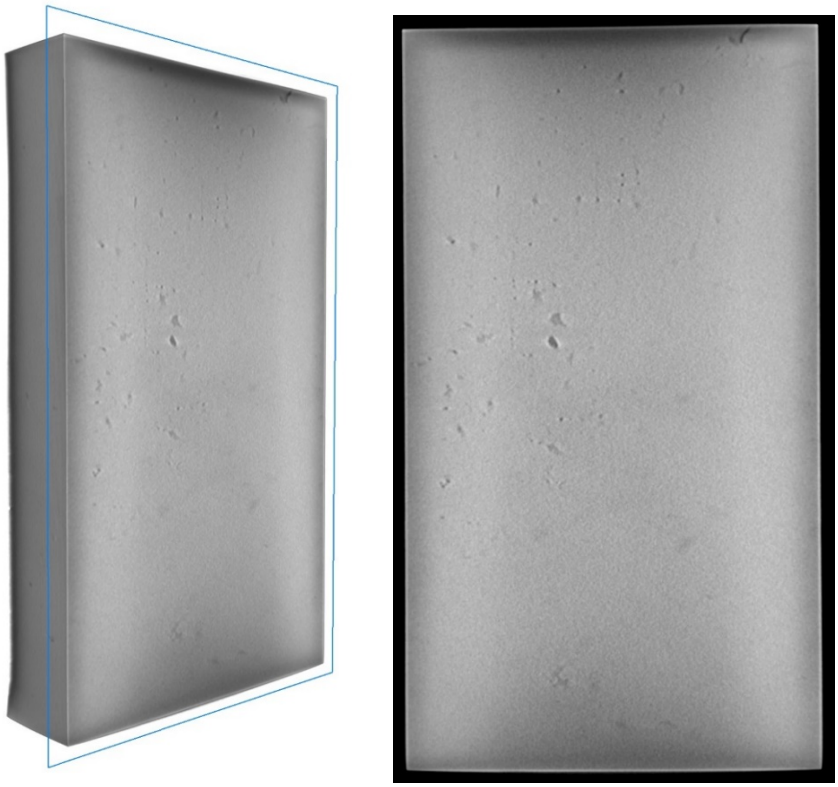

11b. 3-D visualization and 2-D surface about one-quarter of the way through thickness

Fig. 11 3-D sectioned visualizations and corresponding 2-D surface images in interior of specimen SG-10_hatched-tensile parallel to its areal faces



11c. 3-D visualization and 2-D surface about halfway through thickness



11d. 3-D visualization and 2-D surface about three-quarters of the way through thickness

Fig. 11 3-D sectioned visualizations and corresponding 2-D surface images in interior of specimen SG-10_hatched-tensile parallel to its areal faces (continued)



12a. 3-D visualization (left) and 2-D surface (right) close to non-ribbed areal surface

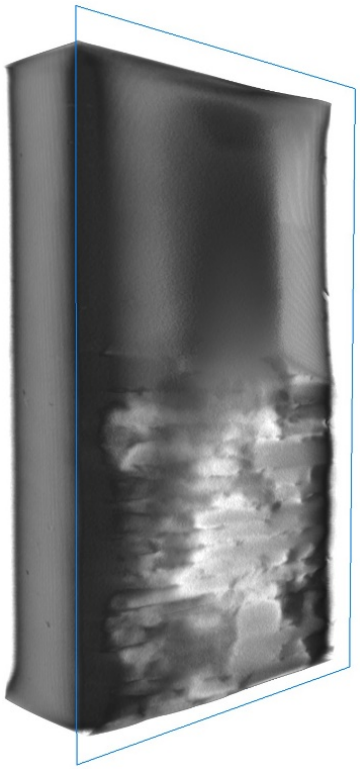

12b. 3-D visualization of outside ribbed areal surface

Fig. 12 3-D sectioned visualization and corresponding 2-D surface image close to non-ribbed areal surface (a) and ribbed surface itself (b) of specimen SG-10_hatched-tensile

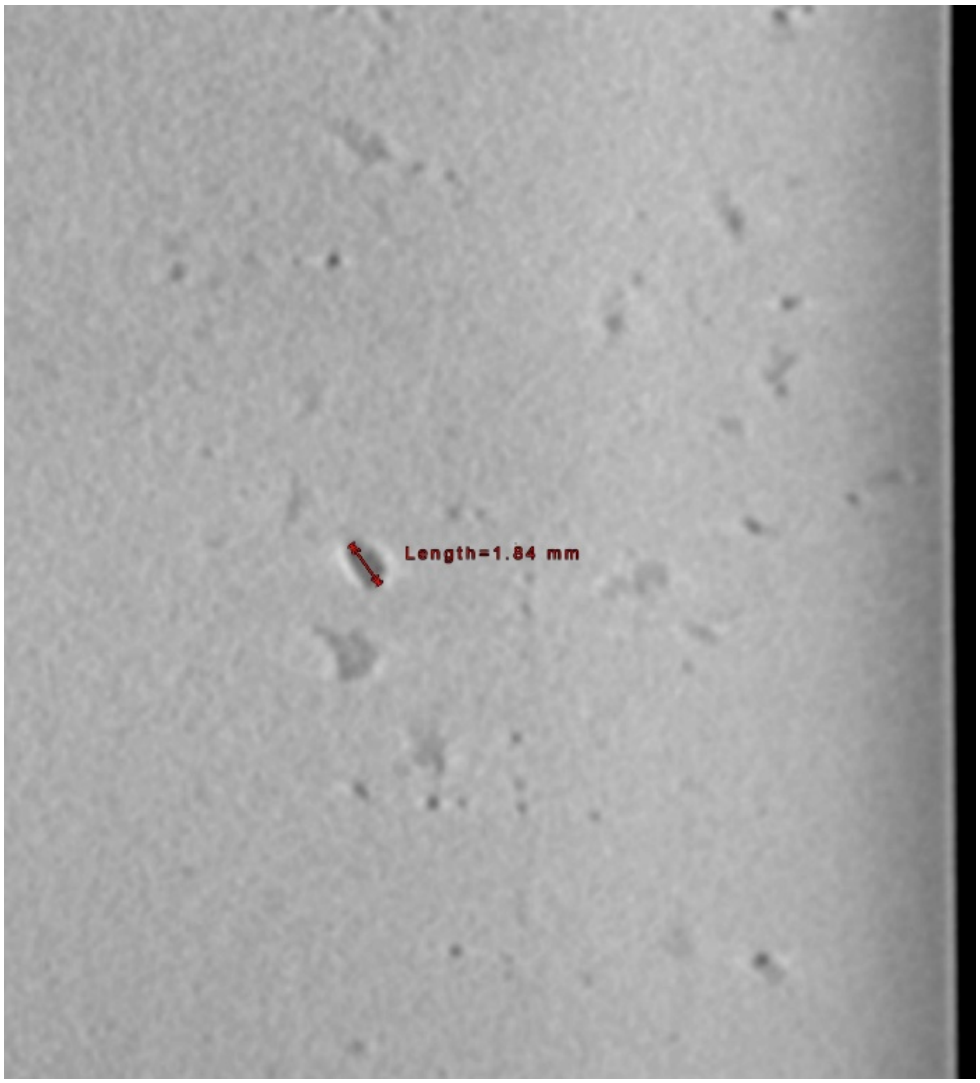

Fig. 13 2-D image of individual porosity/void discontinuity with a maximum dimension of about 1.8 mm in specimen SG-10_hatched-tensile. Note somewhat larger porosity/void almost directly below it.

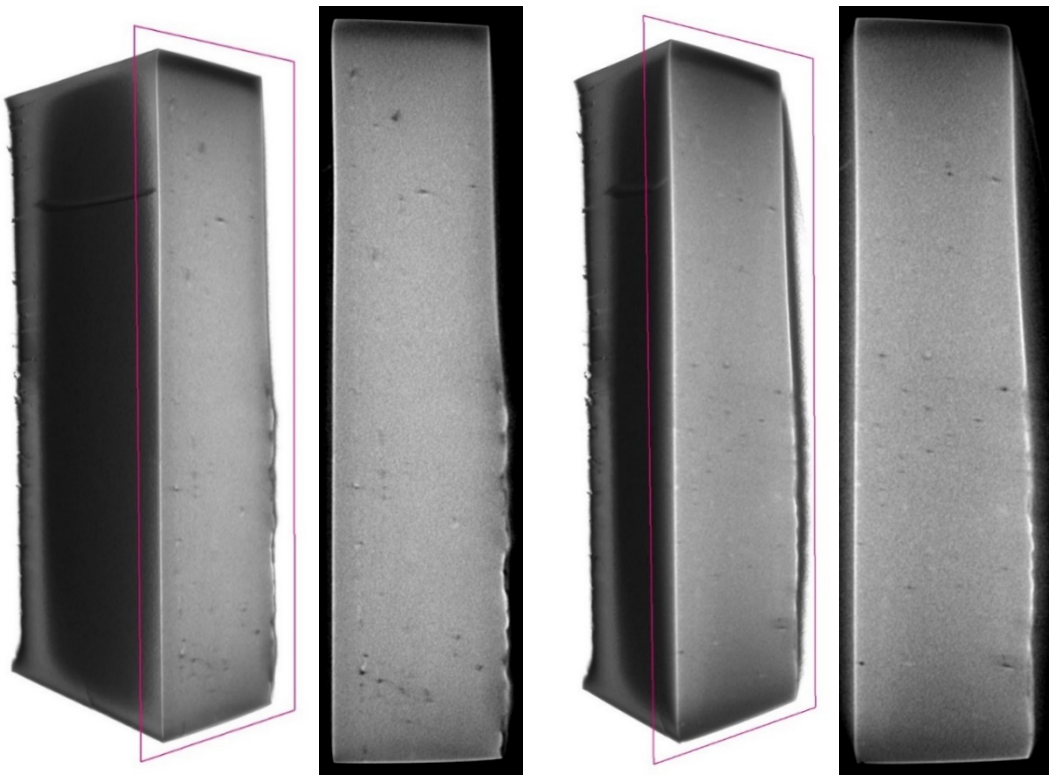

14a. About one-quarter of the way through

14b. About one-half of the way through

14c. About three-quarters of the way through

Fig. 14 3-D sectioned visualizations and corresponding 2-D surface images in interior of specimen SG-10_hatched-tensile perpendicular to its areal faces in short areal direction

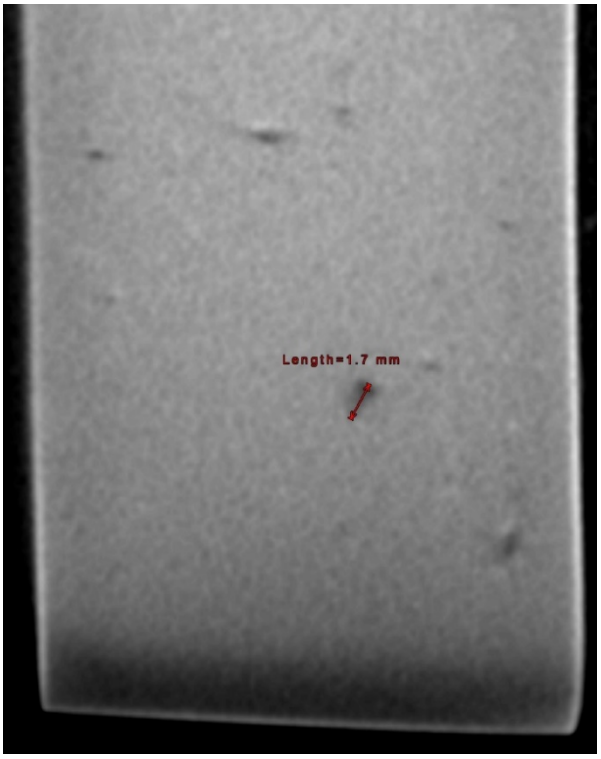

15a. Feature with max dimension of about 1.7 mm

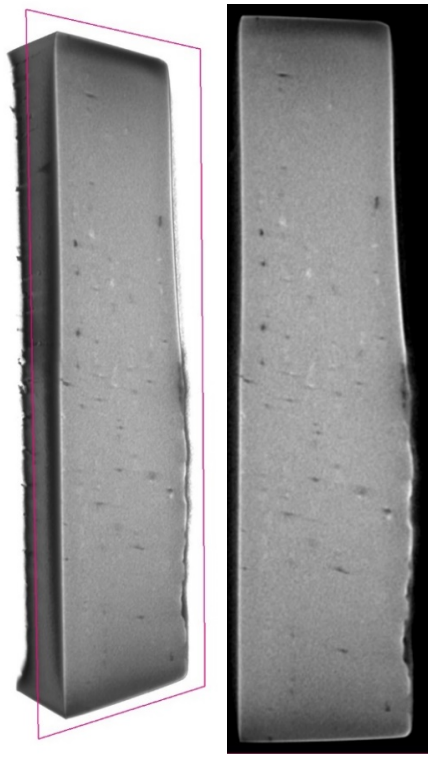

15b. Example of linear ≈ horizontal features in bottom halves of images

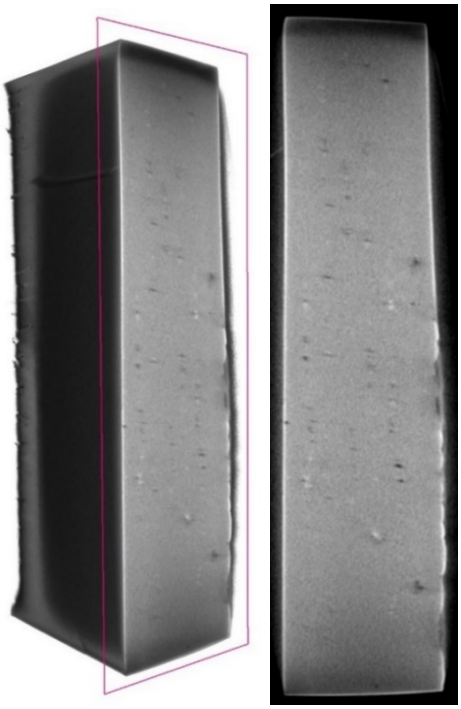

15c. Example of linear ≈ horizontal features throughout images

Fig. 15 Individual porosity/void in middle area (a), and 3-D sectioned and 2-D surface images showing linear approximate horizontal discontinuities (b and c) in interior of SG-10_hatched-tensile

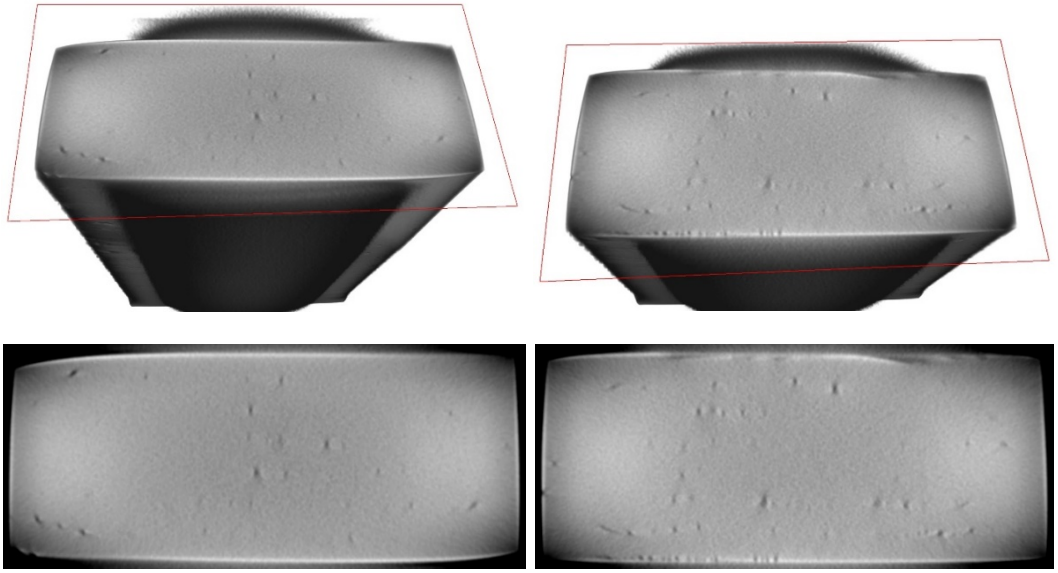

16a. About one-quarter of the way through

16b. About one-half of the way through

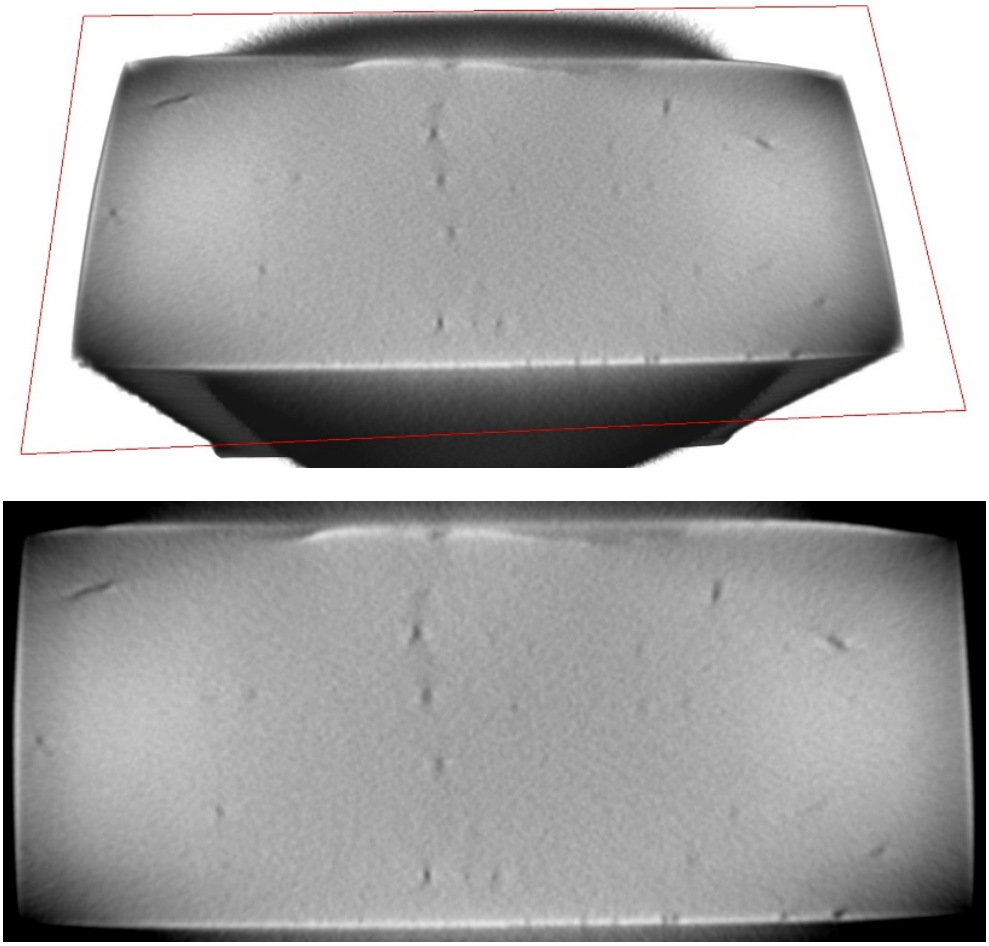

16c. Almost one-half of the way through.

Fig. 16 3-D sectioned visualizations and corresponding 2-D surface images in interior of specimen SG-10_hatched-tensile perpendicular to its areal faces in long areal direction

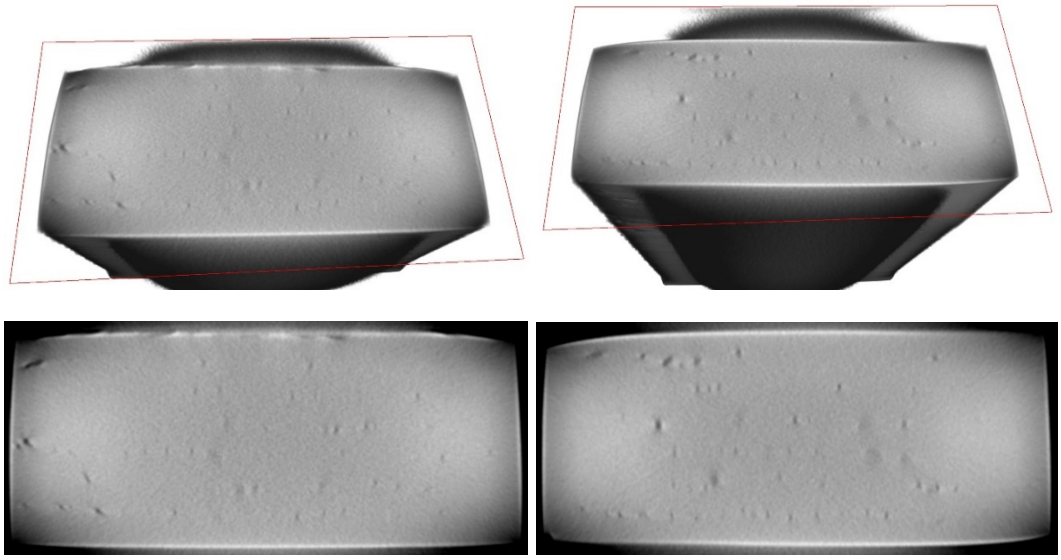

17a. Example of short linear ≈ vertical features near bottom of images.

17b. Second example of short linear ≈ vertical features near bottom of images

Fig. 17 Two different examples of short linear approx. vertical discontinuities in interior of specimen SG-10_hatched-tensile in 3-D visualizations and 2-D surfaces parallel to end faces

5. Summary and Conclusions

Defects in WAAM specimens or components can occur for a variety of reasons, such as poor programming strategy, unstable weld pool dynamics due to poor parameter setup, thermal deformation associated with heat accumulation,[20] environmental influence (such as gas contamination), and other machine malfunctions. Porosity is a common defect that can arise in WAAM processing, and is mainly classified as either a raw-material-induced[21] or process-induced[22] type of defect. Process-induced porosity is usually nonspherical and mainly caused by poor path planning or an unstable deposition process. When the deposition path is complex or the manufacturing process is changeable, insufficient fusion or spatter ejection is easily produced, creating gaps or voids in these influenced regions. Cracking and delamination involve the thermal signature of the manufacturing process as well as the material characteristics of the deposit. Ordinarily, a crack is categorized as either a solidification crack or a grain boundary crack within the WAAM component.[23] The first type of crack depends mainly on the solidification nature of the material and is usually caused by the obstruction of solidified grain flow or high strain in the melt pool.[24] Delamination or separation of adjacent layers takes place due to incomplete melting or insufficient remelting of the underlying solid between layers. Generally, this deficiency is visible and cannot be repaired by postprocess treatment. Given seven different flaw or defect categories, including porosity, cracks, delamination, deformation, oxidation,

residual stress, and surface roughness, WAAM-processed nickel-based maraging steels are about equally susceptible to porosity, delamination, deformation, residual stress, and surface roughness related defects, while being more susceptible to cracking defects and less susceptible to oxidation defects. On a scale of 1–5, with 5 being the most severe susceptibility, nickel-based steels were rated 4 and 1 for cracking and oxidation susceptibility, respectively, with all other defect susceptibilities rated as 3.[7]

Two maraging steel WAAM specimens, named SG-10 "tensile" and SG-10 "hatched-tensile", were mechanically sectioned from larger plates to physical dimensions sufficiently penetrable by the peak kilovoltage of the X-ray technique. Each specimen was CT scanned using 450-kV peak-beam-hardened X-rays. The scanning protocol used both 4X frame averaging and view oversampling to maximize SNR and, thus, image quality as well as minimize noise and the presence of high X-ray attenuation artifacts. Scan data was reconstructed and each specimen was evaluated using 3-D solid internal interrogation and visualization with corresponding 2-D sectioned surface views. The interior of specimen SG-10_tensile had very numerous low-density discontinuities, many of which are probably some type or types of porosity and/or voids. A significant portion of these discontinuities were nonspherical and asymmetric, possibly resulting from process-induced porosity.[7,22] Its interior also had a number of essentially linear, relatively short, horizontal and vertical discontinuities, which are probably the same or similar features as viewed from perpendicularly oriented surfaces that were sometimes roughly grouped spatially or clumped together. The porosity and/or voids and these relatively short crack-like discontinuities in the specimen do not necessarily have the appearance of the same sort of defects that can arise during traditional or standard casting or forging processes, such as gas porosity and different types of shrinkage discontinuities in castings or tears and bursts in forgings. However, as already stated, thermal control over the relatively large volume of liquid weld metal is critical in WAAM processes, and solidification of a large weld pool can thermally behave like solidification of a conventional casting experiencing differences in heating/cooling behavior at different locations in the casting.[16] The relatively short, crack-like discontinuities may have resulted from delaminations or multiple separations of adjacent layers that occurred during the WAAM process.[7] The overall quality of SG-10_tensile is very poor, having extensive porosity and voids as well as the additional possible delaminations or separations. However, the specimen was sectioned from an initial test article fabricated using a non-optimized WAAM process. Given that the purpose of fabricating the test article was to facilitate initial investigation into the capabilities of the WAAM process for this maraging steel material, the high level of discontinuities was not completely unexpected.

The interior of specimen SG-10_hatched-tensile had numerous low-density discontinuities, again many of which are some type of porosity and/or voids but noticeably fewer qualitatively than in SG-10_tensile. As in specimen SG-10_tensile, a significant portion of these discontinuities possibly resulted from process-induced porosity.[7,22] Its interior also had a number of essentially linear approximately horizontal and vertical discontinuities that were sometimes spatially roughly grouped or clumped together, which are also probably the same or similar features as viewed from orthogonal orientations. Also, as with specimen SG-10_tensile, these discontinuities may have resulted from delaminations or multiple separations of adjacent layers that occurred during the WAAM process.[7] However, SG-10_hatched-tensile qualitatively appears to have fewer of these linear discontinuities than SG-10_tensile. The overall quality of SG-10_hatched-tensile is poor with numerous porosity and voids, as well as the additional possible delaminations or separations. It was also sectioned from an initial test article made using a different—but still non-optimized—process than SG-10_tensile. However, the overall quality of specimen SG-10_hatched-tensile is decidedly better than that of specimen SG-10_tensile in terms of both the relative frequency and sizes of porosity and voids and to some extent the presence of the linear delaminations/separations. Even though the quality of specimen SG-10_hatched-tensile is noticeably better than that of specimen SG-10_tensile, but still not free of discontinuities, the level of discontinuities in SG-10_hatched-tensile was not completely unexpected. Improved processes for optimizing the overall quality of maraging steel WAAM-fabricated specimens will be investigated in the future, using results discussed in this report as a guide. Results from XCT scanning and evaluation of new WAAM specimens will be compared with image data of the initial test-article specimens SG-10_tensile and SG-10_hatched-tensile.

6. References

1. American Society for Testing and Materials (ASTM). Standard practice for computed tomographic (CT) examination. Designation: E 1570-95a; 1995.
2. Dennis MJ. Industrial computed tomography: nondestructive evaluation and quality control. In: ASM handbook. Vol. 17. American Society for Metals (ASM) International; 1989.
3. Newton TH, Potts DG, editors. Technical aspects of computed tomography. In: Radiology of the skull and brain. Vol. 5. The CV Mosby Company; 1981.
4. Stanley JH. Physical and mathematical basis of CT imaging. American Society for Testing and Materials (ASTM), ASTM CT Standardization Committee (E7.01.07), ASTM Tutorial: Section 3; 1986.
5. Advanced Manufacturing News Letter. An introduction to wire arc additive manufacturing. 2020 update. p. 1–8. https://amfg.ai/2018/05/17/an-introduction-to-wire-arc-additive-manufacturing/.
6. WAAMMat 2021. Wire + arc additive manufacturing. 2021. p. 1–2. https://waammat.com/about/waam/.
7. Wu B, Pan Z, Ding D, Cuiuri D, Li H, Xu J, Norrish J. A review of the wire arc manufacturing of metals: properties, defects and quality improvement. Journal of Manufacturing Processes. 2018;35:127–139.
8. Ding J, Colegrove P, Mehnen J, Ganguly S, Almeida Sequeira PM, Wang F, Williams S. Thermomechanical analysis of wire and arc additive layer manufacturing process on large multi-layer parts. Comput Mater Sci. 2011;50:3315–3322.
9. Dickens P, Pridham M, Cobb R, Gibson I, Dixon G. Rapid prototyping using 3-D welding. University of Nottingham; 1992. https://repositories.lib.utexas.edu/bitstream/handle/2152/64409/1992-32-dickens.pdf?sequence=2&isAllowed=y.
10. Spencer J, Dickens P, Wykes C. Rapid prototyping of metal parts by three-dimensional welding. Proc Inst Mech Eng Part B J Eng Manuf. 1998;212:175–182.
11. Scott Automation. Reduce costs and increase output with robotic welding. 2018. https://www.scottautomation.com/applications/metal-fabrication welding.

12. Cunningham CR, Flynn JM, Shokrani A, Dhokia V, Newman ST. Invited review article: strategies and processes for high quality wire arc additive manufacturing. Additive Manufacturing. 2018;22:672–686.

13. Muscato G, Spampinato G, Cantelli L. A closed loop welding controller for a rapid manufacturing process. Proceedings of the IEEE International Conference Emerging Technology and Factory Automation (ETFA); 2008. p. 1080–1083.

14. Venturini G, Montevecchi F, Scippa A, Compatelli G. Optimization of WAAM deposition patterns for T-crossing features. Proceedia CIRP. 2016;55:95–100.

15. Mughal MP, Mufti RA, Fawad H. The mechanical effects of deposition patterns in welding-based layered manufacturing. Proc Inst Mech Eng Part B J Eng Manuf. 2007;221(10):1499–1509.

16. Derekar K. A review of wire arc additive manufacturing and advances in wire arc additive manufacturing of aluminum. Materials Science and Technology. 2018;34(8):895–916.

17. Degarmo EP, Black JT, Kohser RA. Materials and processes in manufacturing, 9th ed. Wiley; 2003. p. 119.

18. Muehlhauser B. Optimizing image signal to noise ratio using frame averaging. North Star Imaging Blog; 2015. https://4nsi.com/blog/2015/10/21/optimizing-image-signal-to-noise-ratio-using-frame-averaging/.

19. Shannon CE. Communication in the presence of noise. Proceedings of the Institute of Radio Engineers. 1949;37(1):10–21.

20. Wu B, Ding D, Pan Z, Cuiur, D, Li H, Han J, Fei Z. Effect of heat accumulation on the arc characteristics and metal transfer behavior in wire arc additive manufacturing of Ti6Al4V. J Mater Process Technol. 2017;250:304–312.

21. Busachi A, Erkoyuncu J, Colegrove P, Martina F, Ding J. Designing a WAAM based manufacturing system for defense applications. Procedia CIRP. 2015;37:48–53.

22. Sames WJ, Medina F, Peter WH, Babu SS, Dehoff RR. Effect of process control and powder quality on Inconel 718 produced using electron beam melting. Proceedings of the 8th International Symposium on Superalloy 718 and Derivatives. John Wiley and Sons; 2014. p. 409–423.

23. Sames WJ, List F, Pannala S, Dehoff RR, Babu SS. The metallurgy and processing science of metal additive manufacturing. Int Mater Rev. 2016;61:315–360.

24. TWI Ltd. What is hot cracking (solidification cracking). 2017. http://www.twi-global.com/technical-knowledge/faqs/material-faqs/faq-what-is-hot-cracking-solidification-cracking/.

List of Symbols, Abbreviations, and Acronyms

2-D	two-dimensional
3-D	three-dimensional
AM	additive manufacturing
f(x)	temporal (or spatial) continuous function
kV	kilovoltage
MIG/MAG	metal inert gas/metal active gas
NDE	nondestructive evaluation
R&D	research and development
SEMD	Sciences of Extreme Materials Division
SNR	signal-to-noise ratio
WAAM	wire arc AM
WMRD	Weapons and Materials Research Directorate
XCT	X-ray computed tomography
X_{max}	maximum spatial frequency

1 (PDF)	DEFENSE TECHNICAL INFORMATION CTR DTIC OCA
1 (PDF)	DEVCOM ARL FCDD RLD DCI TECH LIB
3 (PDF)	DEVCOM ARL FCDD RLW MB W GREEN B LOVE FCCD RLW S V CHAMPAGNE
1 (PDF)	SOLVUS GLOBAL A BIRT